

Molecular-Level Details of Morphology-Dependent Exciton Migration in Poly(3-hexylthiophene) Nanostructures

Patrick C. Tapping, Scott N. Clifton, Kyra N. Schwarz,^a Tak W. Kee, and David M. Huang*

Department of Chemistry, The University of Adelaide, South Australia 5005, Australia

E-mail: david.huang@adelaide.edu.au

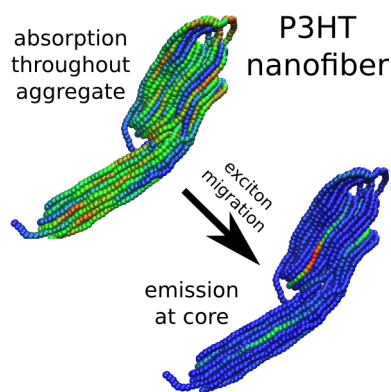
Phone: +61-8-8313-5580

^aCurrent address: School of Chemistry, University of Melbourne, Parkville, VIC, 3010 Australia

Abstract

The morphology dependence of exciton transport in the widely used conjugated polymer poly(3-hexylthiophene) (P3HT) is elucidated by combining an accurate mesoscale coarse-grained molecular dynamics simulation model of P3HT structure with a Frenkel–Holstein exciton model. This model provides a more realistic representation than previously achieved of the molecular-level details of exciton transport on large length scales relevant to electronic applications. One hundred 300-monomer regioregular P3HT chains are simulated at room temperature for microseconds in two implicit solvents of differing solvent quality in which the polymer chains adopt contrasting morphologies: nanofiber-like aggregates or well-separated extended conformations. The model gives reasonable quantitative agreement with steady-state absorption and fluorescence and time-resolved fluorescence experiments, and provides valuable insight into the mechanism of exciton transport in conjugated polymers. In particular, exciton transfer in nanofiber aggregates is shown to occur mainly through interchain hops from chromophores on the aggregate surface towards the aggregate core, a behavior with important

implications for organic electronic applications. Furthermore, the counterbalancing effects of greater orientational order and faster exciton transport in nanofiber aggregates than in extended chains is found to explain the puzzling observation of similar fluorescence anisotropy decay rates in nanofibers and free chains.



Keywords

P3HT, conjugated polymer, nanofiber, organic photovoltaics, energy transfer

*To whom correspondence should be addressed

Introduction

The study of conjugated polymers is motivated by their use as electron donor or acceptor materials in the active layers of organic electronic devices such as solar cells¹ and light-emitting diodes.² Despite efficiencies of organic solar cells lagging behind those of conventional silicon devices, organic devices remain appealing because of their low-temperature and solution-based fabrication, which allows flexible and transparent solar cells to be made using low-cost high-throughput production methods.^{3,4} Nevertheless, efficiency improvements would help to encourage the more widespread adoption of organic photovoltaics.⁵

The microstructure of the bulk heterojunction — the bicontinuous network of donor and acceptor materials in the active layer — has been shown to play a crucial role in charge generation, separation, and transport in organic solar cells, and hence in the overall device efficiency.^{6–9} Developing a comprehensive understanding of the effects of bulk heterojunction morphology on device performance is challenging, given the crucial role that polymer structure on a wide range of length scales — from the molecular level up to the device scale — has on electronic properties.¹⁰

Theory and computation can provide valuable insight into the role of bulk heterojunction morphology in controlling device performance and could eventually lead to the rational design of organic solar cells. Most computational approaches to addressing the morphology dependence of the electronic properties of conjugated polymers and polymer-based devices fall into one of two classes, neither of which has been entirely satisfactory in treating the range of length scales that are important in conjugated-polymer devices. On the one hand are models in which the polymer structure is represented in full atomistic detail and electronic properties are computed using quantum chemical methods.^{11–17} While such models are generally accurate, the high computational expense limits their use to systems of up to hundreds of atoms, and so polymer conformations cannot be effectively simulated. On the other hand are con-

tinuum or lattice models, in which the polymer structure and exciton or charge transport are described by a reduced set of variables on a grid.^{18–23} Although simulations on experimental length and time scales are readily accessible using such models, molecular-level structure and chain topology are neglected.

Between these two extremes are mesoscale coarse-grained models in which groups of atoms are represented by a smaller number of interaction sites, allowing multiple chains of thousands of monomers to be feasibly simulated while retaining details about chain connectivity that are crucial to energy and charge-transport mechanisms.^{24–29} However, previous calculations of this nature have used rather approximate models of polymer structure, with conformations usually generated from a random distribution and solvent effects neglected, which is unlikely to provide an accurate representation of the complexity of a real system.

In this work, we address this issue by starting with realistic structures of the polymer poly(3-hexylthiophene) (P3HT), obtained using an accurate, coarse-grained molecular dynamics model parametrized to reproduce the local structure and dynamics of an atomistic P3HT model.³⁰ Large multi-chain systems are simulated in two different solvents in which the P3HT chains adopt two conformationally distinct morphologies. P3HT was one of the first conjugated polymers used in the manufacture of organic solar cells³¹ and is one of the most widely studied conjugated polymers, with over 1,400 scientific publications on this polymer in 2014 alone, according to Web of Science. P3HT readily exists in a variety of morphologies including amorphous bulk phases, nanoparticles, and semicrystalline nanofibers, which has significant effects on its physical, optical, and electronic properties.^{32–35} We then use a Frenkel–Holstein exciton model^{27,28,36,37} to determine the locations and energies of chromophores — a method that scales reasonably up to hundreds of polymer chains — in polymer conformations extracted from the coarse-grained molecular dynamics simulations. Finally, we perform kinetic Monte Carlo simulations of inter-chromophore exciton transfer using trans-

fer rate coefficients derived from the Fermi Golden Rule, assuming a point-dipole approximation for inter-monomer interactions. We verify that the simulations reproduce experimental measurements and use them to provide new molecular-level insight into the mechanism of exciton migration through self-assembled P3HT nanostructures.

Computational Methods

Coarse-grained Molecular Dynamics

The solution-phase structure of P3HT was simulated using molecular dynamics of a coarse-grained polymer model, which has been described in detail in a previous publication.³⁰ Briefly, each hexylthiophene monomer was represented by a set of three spherical beads corresponding to the centers-of-mass of the thiophene ring and the first three methyl groups and last three methyl groups of the hexyl sidechain, respectively. This atomistic-to-coarse-grained mapping is shown diagrammatically in Figure 1a. Simulations of the polymers were carried out in implicit solvent using Langevin dynamics at constant volume and temperature, with the interactions between coarse-grained sites parametrized so as to match the local structure and dynamics measured in constant-pressure simulations of an atomistic model of P3HT in an explicit solvent, anisole. This coarse-grained P3HT model was found to agree with the experimental phase behavior of P3HT in anisole, showing a transition between a non-aggregated and aggregated state as the temperature dropped below around 35 °C.³⁰ The size of the simulated aggregates also matched the widths of P3HT nanofiber aggregates measured experimentally. To model P3HT in a better solvent than anisole (e.g. tetrahydrofuran (THF)) in which the polymer chains are fully solvated and form extended structures at room temperature, the non-bonded polymer-polymer pair interactions were reduced by 10% of their value in the coarse-grained P3HT model in implicit anisole.

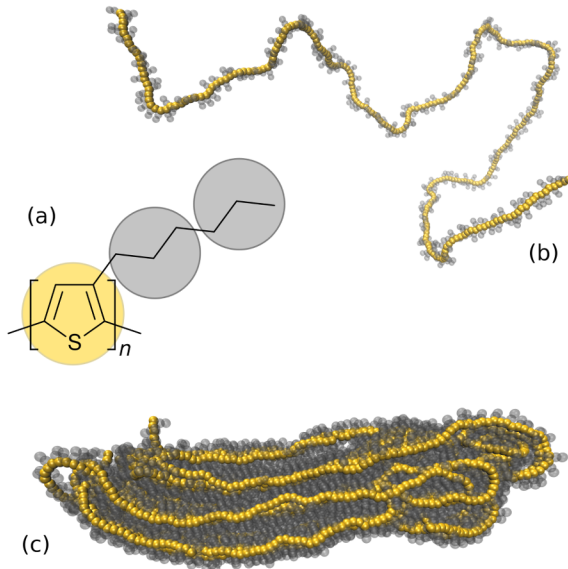


Figure 1: (a) Mapping of P3HT atomistic to coarse-grained sites and example structures of (b) a free chain and (c) a nanofiber aggregate. The polythiophene backbone is indicated in yellow, with the alkyl sidechain units shown in gray. The view of the nanofiber is looking down through the π -stacking direction, showing the alkyl sidechain interactions.

For convenience, we will refer to the simulations at room temperature of P3HT in implicit anisole and of P3HT in the better solvent as “nanofiber” and “free chain” simulations, respectively, to describe the polymer morphologies formed in these simulations. Note that the nanofiber aggregates simulated are not entire nanofibers as would be produced experimentally, but instead constitute several π -stacked layers in a section of a nanofiber.³⁰ Examples of the coarse-grained structures that result from these two solvent models are shown in Figures 1b and c. Both the nanofiber and free chain systems consisted of one hundred 300-monomer P3HT chains in a cubic simulation box with periodic boundary conditions enforced. Simulations were carried out at constant volume and temperature using Langevin dynamics, starting from an initial configuration of randomly placed and oriented chains with inter-monomer dihedral angles selected from a Boltzmann distribution of the inter-monomer torsional potential. The temperature was set to 293 K.

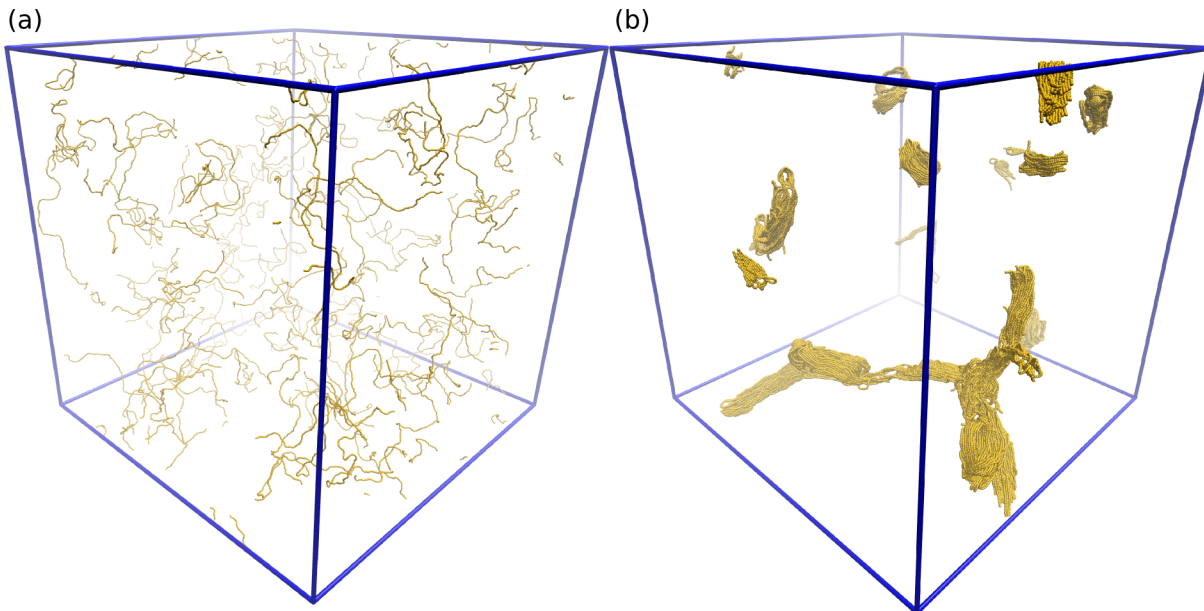


Figure 2: Snapshots from molecular dynamics simulations of 100 P3HT (a) free chains in good solvent and (b) nanofiber aggregates formed in a marginal solvent (anisole) at 0.13 and 1.0 wt% P3HT concentration respectively. For clarity, alkyl sidechains are not shown.

Nanofiber simulations were carried out at three different P3HT concentrations with total system volumes of 6.7×10^6 , 9.8×10^5 , and $4.3 \times 10^5 \text{ nm}^3$ for 2480, 1040, and 240 ns, respectively, to model 0.13, 1.0, and 2.0 wt% systems in anisole. P3HT has been shown experimentally to form nanofibers in anisole at concentrations between 0.005 and 1.0 wt%.³⁸ The 1.0 and 2.0 wt% simulations were started from configurations obtained by rapidly compressing the configuration of the 0.13 wt% simulation after $1.76 \mu\text{s}$ in a constant pressure simulation over a period of 0.5 ns. A single free chain simulation was carried out for 544 ns with the same system volume as the 0.13 wt% nanofiber system. It was verified that any measured quantities discussed below ceased to display systematic variations with time within the time scale of the simulations. Figure 2 shows examples of the resulting configurations for the free chain (Figure 2a) and nanofiber (Figure 2b) systems.

The friction coefficient for the Langevin dynamics in the nanofiber simulations was reduced by a factor of 10 from the value in Ref. 30 to accelerate nanofiber formation. While such a change would affect the dynamics of chain aggregation, it should not impact the thermodynamic stability of the polymer structures

formed. Furthermore, both cases correspond to “high” friction in the context of aggregation dynamics, with the time scale of decorrelation of particle velocities in both cases being much shorter than the time scale of aggregation; as such, aggregation in both cases should occur by a similar mechanism of diffusive motion biased by inter-particle interactions.

Exciton Transport Simulations

Frenkel–Holstein Exciton Model

Exciton transport was simulated using a Frenkel–Holstein model developed by Barford and Tozer,^{28,36} which accounts for the effects of molecular-level polymer structure on excitation energies and dynamics. Here, it was applied to chains representing P3HT generated from the coarse-grained molecular dynamics simulations described above. The main features of the model as they apply to the present work are given below.

The Frenkel exciton model treats the electron–hole pair as a single particle that can be delocalized in one dimension along the polymer chain.^{39,40} The Frenkel–Holstein model extends the Frenkel model by coupling the exciton to the motion of the nuclei in the polymer.^{41–44}

The nuclei are treated classically, considering their motion to be described by a single normal coordinate. In P3HT, the dominant normal coordinate is linked to the C=C stretching mode, as discussed below. The coupling to the normal mode simulates the relaxation process from the vertically excited state with the initial ground state geometry, to the excited but vibrationally relaxed state with the corresponding change in nuclear coordinates.

The Frenkel–Holstein Hamiltonian is

$$H = \sum_i (E_0 + \alpha_i - A\hbar\omega Q_i) \hat{a}_i^\dagger \hat{a}_i + \sum_{i>j} J_{ij} (\hat{a}_i^\dagger \hat{a}_j + \hat{a}_i \hat{a}_j^\dagger) + \frac{\hbar\omega}{2} \sum_i Q_i^2, \quad (1)$$

where i and j are numeric labels of the monomer units in a chain and the operators \hat{a}_i^\dagger and \hat{a}_i respectively create or destroy an exciton on monomer i . The on-site excitation energy is given by $(E_0 + \alpha_i)$, where α_i is a Gaussian random variate with standard deviation σ_α , representing energetic disorder caused by local structural fluctuations in the polymer system.^{36,45} The electronic coupling between monomers i and j is described by J_{ij} . We only consider nearest-neighbor interactions ($j = i \pm 1$) in eq 1, which are expected to be dominant,²⁷ for which this term can be decomposed into two components,

$$J_{ij} = J^{\text{DD}} + J^{\text{SE}} \cos^2(\phi_{ij}). \quad (2)$$

J^{DD} is the through-space dipole–dipole coupling, for which the orientational and distance dependence between adjacent monomers is considered negligible. J^{SE} is the through-bond superexchange contribution, which is modulated by $\cos^2(\phi_{ij})$, where ϕ_{ij} is the dihedral angle between monomers i and j . In this way the planar arrangement of monomer units equates to maximum π -conjugation and therefore minimizes the excitation energy. The coupling of the exciton to the normal coordinate is described by the exciton–phonon coupling parameter, A , with Q_i being the dimensionless displacement at site i associated with the normal mode with angular frequency ω . The eigenstates of eq 1

define the wavefunctions of the exciton center-of-mass particle, with the corresponding eigenvalue giving the energy for the state.

When there is no coupling to the normal coordinate ($Q_i = 0$), eq 1 reduces to the Frenkel Hamiltonian, which is used to determine the vertically excited states. The lowest energy eigenstates of eq 1 define the absorbing chromophores, or local exciton ground states (LEGSs), and therefore can be identified as those eigenstates that satisfy the inequality

$$\left| \sum_i \psi_{mi} |\psi_{mi}| \right| \geq 0.95, \quad (3)$$

where ψ_{mi} is the value of the wavefunction of state m on monomer i .⁴⁶ This criterion selects states for which 95% of the wavefunction density is in the main peak of the wavefunction and therefore discriminates against those states whose wavefunctions change sign and have both significant positive and negative amplitudes. The remaining higher-energy states describe local exciton excited states (LEESs), which have nodes but span the same chain segments as LEGSs, and quasi-extended exciton states (QEESs), which have nodes and spatially overlap more than one LEGS. These higher energy states contribute to the simulated absorption spectrum, but upon excitation are assumed to relax rapidly to the LEGS with maximum wavefunction overlap.⁴⁷ Note that for the monomer basis used to describe the eigenstates of the Hamiltonian in eq 1, a system of N monomers generates N eigenstates, which include both LEGSs and higher lying excited states. As a consequence, the number of LEGSs is generally significantly smaller than the number of eigenstates. An example of the wavefunctions of the LEGSs found on a P3HT chain is shown in Figure 3.

Coupling to the normal coordinate ($Q_i \neq 0$) gives the wavefunctions and energies of electronically excited but vibrationally relaxed chromophores. This process is greatly simplified by assuming that the wavefunction is identical to that of the vertically excited state. This assumption has been validated by density matrix renormalization group calculations per-

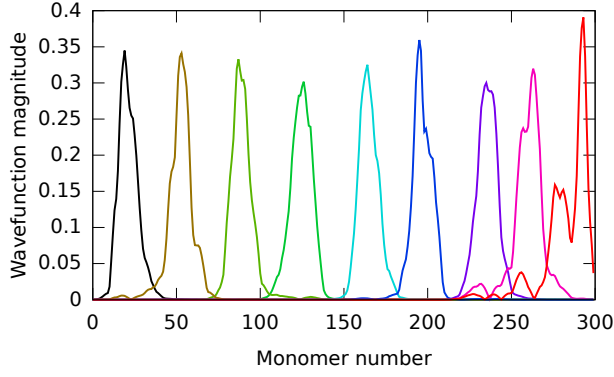


Figure 3: Computed wavefunction magnitudes for LEGSs on a 300-monomer polymer chain. The nine different states in this particular case are color-coded for clarity.

formed by Marcus et al. on a Frenkel–Holstein model of disordered poly(*para*-phenylene) and by Barford and Tozer on poly(*para*-phenylenevinylene).^{28,37} These calculations showed minimal variance between the wavefunctions of the vertically excited and vibrationally relaxed states. In the large-polaron limit applicable to conjugated polymers, the dimensionless displacement of monomer i depends on the exciton density in state m according to^{27,42}

$$Q_{mi} = A|\psi_{mi}|^2. \quad (4)$$

As ψ_{mi} is assumed to be equal to the previously determined wavefunction of the LEGS m , the final term in eq 1 can thus be used to directly compute the vibrational relaxation energy,

$$E_{rm} = \frac{A^2\hbar\omega}{2} \sum_i |\psi_{mi}|^4, \quad (5)$$

and therefore the energy of the emissive chromophores.

Exciton Localization

The exciton center-of-mass, \mathbf{R}_m , for each LEGS m can be determined from the wavefunctions by

$$\mathbf{R}_m = \sum_i \mathbf{R}_i \psi_{mi}^2, \quad (6)$$

where \mathbf{R}_i is the spatial position of monomer i . The root-mean-squared deviation of the wavefunction along the polymer chain is used to find

the localization length and therefore effective conjugation length, l_m , of the chromophore m by

$$l_m = \left(\frac{12\pi^2}{\pi^2 - 6} \right)^{\frac{1}{2}} \left[\sum_i i^2 \psi_{mi}^2 - \left(\sum_i i \psi_{mi}^2 \right)^2 \right]^{\frac{1}{2}}, \quad (7)$$

as described by Makhov and Barford.⁴⁸

Monte Carlo Hopping Simulations

Exciton transport in the model occurs through a Förster-type resonance energy transfer process.^{12,13,49} With the location and energy of the absorbing or acceptor and emissive or donor chromophores determined *via* the Frenkel–Holstein model, the nonradiative energy transfer rate between each donor and acceptor can be calculated. The transfer rate between a donor and acceptor pair, k_{DA} , depends on the distance between the chromophores and the alignment of their transition dipole moments as well as the spectral overlap of the donor and acceptor, and is calculated using the Fermi Golden Rule,

$$k_{DA} = \frac{2\pi}{\hbar} J_{DA}^2 X_{DA}. \quad (8)$$

The electronic coupling between the donor (D) and acceptor (A) chromophores, which is assumed to comprise point-dipole interactions between monomers on the different chromophores not accounted for in the nearest-neighbor Hamiltonian (eq 1), is taken as²⁸

$$J_{DA} = \frac{\mu_0^2}{4\pi\epsilon_r\epsilon_0} \sum_{\substack{D_i \\ A_j \\ i \neq j}} \frac{\hat{\mathbf{r}}_i \cdot \hat{\mathbf{r}}_j - 3(\hat{\mathbf{R}}_{ij} \cdot \hat{\mathbf{r}}_i)(\hat{\mathbf{R}}_{ij} \cdot \hat{\mathbf{r}}_j)}{|\mathbf{R}_i - \mathbf{R}_j|^3} \psi_{Di} \psi_{Aj}, \quad (9)$$

where μ_0 is the magnitude of the transition dipole moment of a single monomer, ϵ_r is the relative permittivity of the polymer, $\hat{\mathbf{r}}_i$ is a unit vector in the direction of the transition dipole moment of monomer i , which is assumed to be oriented along the line joining the adjacent monomer centers,⁵⁰ and $\hat{\mathbf{R}}_{ij}$ is a unit vector between monomers i and j . This equation is equivalent to the line-dipole approximation for Coulombic coupling between chromophores, which gives good agreement with exact results for short chains for inter-chromophore distances

more than twice the inter-monomer distance and is essentially exact for all chain lengths when the inter-chromophore distance exceeds three times the inter-monomer distance.⁵¹ Most of the chromophores in our simulations satisfy the latter condition. This approximation may not be so accurate for adjacent π -stacked chromophores in polymer aggregates. We have compared the excitonic coupling between two ordered π -stacked P3HT decamers separated by 3.9 Å in the π -stacking direction from our model with the value from accurate transition density cube (TDC) calculations,⁵² and found that our model overestimates the coupling by 50%. On the other hand, our coarse-grained molecular dynamics model overestimates the π -stacking distance in P3HT slightly compared with experiment,³⁰ resulting in an underestimate of the coupling of around 15% for typical π -stacking distances compared with the TDC calculations. Thus, we expect the excitonic couplings to reproduce reasonably well those in the real system.

Spectral overlap of the donor with the acceptor, X_{DA} , is calculated by treating the donor emission and acceptor absorption spectra as two-level Franck–Condon progressions, with lines replaced by Lorentzian distributions with FWHM of 0.1 eV.^{53–55} The effective Franck–Condon factor, F_m , for transitions to the v th vibrational level of chromophore m is determined by

$$F_m = \frac{e^{-S_m} S_m^v}{v!}, \quad (10)$$

where S_m is the Huang–Rhys parameter for chromophore m , related to the chromophore length by

$$S_m = \frac{A^2}{2} \sum_i |\psi_{mi}|^4. \quad (11)$$

Competing with exciton hopping is radiative decay from the donor chromophores. The radiative rate is determined by

$$k_r = \frac{n |\boldsymbol{\mu}_m|^2 E^2}{3\pi\epsilon_0 \hbar^4 c^3}, \quad (12)$$

where n is the refractive index of the pure poly-

mer, $\boldsymbol{\mu}_m = \mu_0 \sum_i \hat{\mathbf{r}}_i \psi_{mi}$ is the total transition dipole moment of chromophore m , and E is the relaxed energy of the chromophore, which is equivalent to the energy of the emitted photon.

Note that only excitation of and energy transfer between local exciton ground states (LEGSs) and the corresponding vibrationally relaxed states is considered in this model. Exciton transfer may not occur exclusively through LEGSs, but this transport mechanism is expected to dominate for several reasons. Firstly, as previously mentioned, these higher excited states are expected to relax rapidly to LEGSs on time scales (~ 10 s to 100s of fs²⁷) much shorter than the time scale of exciton hopping (10s of ps). Secondly, the transition dipole moments (and hence oscillator strengths) of these higher excited states, due to the oscillatory nature of their node-containing wavefunctions, will be smaller than those of the LEGSs,^{37,46} so absorption probabilities and exciton transfer rates involving these higher excited states will be correspondingly smaller than those involving LEGSs, particularly for less coiled chains.³⁷ Finally, following the initial excitation, after which the exciton rapidly finds itself in a LEGS for the reasons mentioned above, further exciton transfer will occur to other LEGSs as the higher lying excited states are energetically inaccessible to the generally energetically downhill exciton transfer process.

The initially excited chromophore is randomly selected with a probability dependent on the degree of spectral overlap of the acceptor with the simulated laser excitation wavelength. At each state, the exciton may either hop to a new site or recombine radiatively. A set of time intervals for these events is determined by $\Delta t = -\ln x/k$, where $k = \{k_{\text{DA}}, k_r\}$ is the set of all rate constants for that donor and x is a random uniform deviate in the interval $[0, 1]$ chosen for each k . The event with the lowest Δt is then selected as the transition to the new state. If the transition is a nonradiative hop to a new chromophore, then the process continues until radiative decay occurs.

The free chain simulation used 68 configurations taken at 8 ns intervals after an 8 ns equilibration period. The nanofiber system com-

binned 63, 130, and 30 configurations of the 0.13, 1.0, and 2.0 wt% systems, respectively, taken at 8 ns intervals after an 1.98 μs period of fiber formation. Each timestep from the free chains and nanofibers was processed 14 and 4 times, respectively, to give ~ 1000 configurations for each system. Note that a single configuration will give slightly different chromophore boundaries and energies on each run due to the diagonal disorder α present in the Frenkel–Holstein Hamiltonian. No significant differences in the results were observed when the different concentration nanofiber systems were processed individually. For each configuration, 10^5 excitations were performed.

Model Parametrization

The parameters used in the Frenkel-Holstein model for P3HT are summarised in Table 1. The parameters E_0 , J^{DD} , J^{SE} , and μ_0 were determined *via* quantum chemical calculations of methylthiophene oligomers. The hexyl sidechains of P3HT were replaced with methyl groups to reduce computational complexity, as this does not affect the electronic properties of the oligomers significantly, which are dominated by the backbone conjugation.^{56,57} Structures were geometry optimised using the AM1 method and the $S_0 \rightarrow S_1$ transition energies computed using ZINDO/S.

The transition energies from ZINDO/S calculations of 3-methylthiophene oligomers agree reasonably well with the energies of the absorption maxima for the $S_0 \rightarrow S_1$ transition of thiophene oligomers in benzene solution⁵⁸ and of 3-octylthiophene oligomers in chloroform.⁵⁹ Because relatively little energy (compared with $k_{\text{B}}T$) is required to change the conformation of 3-methylthiophene oligomers significantly from the minimum-energy conformer in which the thiophene rings are coplanar,³⁰ the calculations were carried out for oligomers whose inter-monomer dihedral angles had been selected randomly from a Boltzmann distribution in the dihedral potential at 298 K.³⁰ As shown in the Supporting Information, although the calculations underestimate the experimental dimer transition energy by around 0.2 eV,

for longer oligomers the calculations and experiments for thiophene oligomers agree within error. Thus, the parameters obtained from the ZINDO/S calculations for the on-site excitation and nearest-neighbor coupling energies are expected to be reasonably accurate.

The value of J^{SE} was found by the difference in transition energies of methylthiophene dimers with dihedral angles of 180° (planar) and 90° (orthogonal) (see Supporting Information). To determine E_0 and J^{DD} , the transition energies of oligomers of length 5 to 30 were plotted against the inverse of the number of thiophene units. The equivalent planar coarse-grained structures were built and the transition (LEGS) energies determined using the Frenkel exciton model with the values of $(J^{\text{DD}} + J^{\text{SE}})$ and E_0 selected to match, respectively, the slope and intercept from the quantum calculations (see Supporting Information).

The transition dipole moment of a single monomer, μ_0 , was determined by plotting the square of the transition dipole moment for methylthiophene oligomers of length 10 to 30 against the number of thiophene units. The linear fit was then extrapolated back to give the magnitude of the transition dipole moment of a single unit.

The refractive index of the pure polymer, n , was obtained from spectroscopic ellipsometry measurements of P3HT films.⁶⁰ For simplicity we have ignored the wavelength dependence of the refractive index of P3HT. The selected value is a good estimate for regiorandom P3HT; the refractive index for regioregular P3HT is more heavily wavelength dependent.

In P3HT the energy of the primary normal mode, $\hbar\omega$, corresponds to the C=C stretch at 1450 cm^{-1} (0.18 eV) that is observed in Raman spectra of P3HT films⁶¹ and in the single-molecule absorption spectrum.⁴⁴ The shoulders seen in the UV-visible absorption spectrum of P3HT nanofibers (Figure 4) also correspond to this value.

The value for the exciton–phonon coupling parameter, A , was chosen to match the experimentally observed relaxation energy (Stokes shift), and is similar to values used by Barford et al. in exciton transfer simulations of MEH-

Table 1: Summary of parameters used in exciton transport model for P3HT

	parameter	value
E_0	Nominal on-site excitation energy for a single monomer	5.70 eV
σ_α	Standard deviation of on-site excitation energy due to local disorder	0.065 eV
J^{DD}	Nearest neighbor exciton transfer integral: dipole–dipole contribution	−0.95 eV
J^{SE}	Nearest neighbor exciton transfer integral: through bond superexchange contribution	−0.80 eV
μ_0	Dipole moment of a single monomer	2.05×10^{-29} C m
$\hbar\omega$	Energy of normal mode of angular frequency ω	0.18 eV
A	Exciton–phonon coupling	4.5
n	Refractive index of polymer, $n = \sqrt{\epsilon_r}$	1.75

PPV.³⁶

Experimental Methods

Free chains of P3HT in solution were prepared by dissolving regioregular P3HT (Rieke Metals, MW = 50 000 g mol^{−1}, 99% regioregularity) in THF (Scharlau) by sonication at 25 °C for one hour to produce 0.1 g L^{−1} solutions, which were filtered through a 0.2 μm nylon filter. Nanofibers of P3HT were produced by precipitation from anisole (Merck) at a concentration of 0.5 g L^{−1} using the whisker method described by Samitsu et al.³⁸

Steady-state absorption spectra were obtained on a Cary 300 UV-visible absorption spectrophotometer using a 1 cm path length quartz cuvette and the free chain or nanofiber solution diluted to 0.01 g L^{−1} in THF or anisole, respectively. Fluorescence spectra were obtained using the same solutions on a Perkin-Elmer LS-55 fluorescence spectrometer with an excitation wavelength of 400 nm and excitation and emission slit widths set at 5 nm.

Time-resolved fluorescence was measured using a fluorescence upconversion spectrometer (Halcyone, Ultrafast Systems). A continuous wave 532 nm Nd:YVO₄ laser at 8 W (Millenia Prime, Spectra-Physics) pumped a mode-locked Ti:Sapphire oscillator (Tsunami, Spectra-Physics) to produce 800 nm pulses at a rate of 80 MHz. A pulse picker selected pulses at a rate of 40 MHz that were then split into

excitation and gate beams. The excitation wavelength of 400 nm was generated by doubling of the oscillator output using a BBO crystal. For the isotropic emission experiments, the gate pulse polarization was set to the magic angle (54.7°) with respect to the excitation pulse. Anisotropy measurements were calculated from alternate scans with the gate pulse parallel or perpendicular to the excitation, with anisotropy defined as $r(t) = \frac{I(t)_\parallel - I(t)_\perp}{I(t)_\parallel + 2I(t)_\perp}$. Each experiment consisted of the averaging of three runs. For each delay time point a three second sampling time was used for a total of 1.2×10^8 laser excitations. Measurements were taken in a 2 mm quartz cuvette (Starna Cells 21-Q-2) at a concentration of 0.02 g L^{−1} and stirred throughout the duration of the experiments. No photodegradation of the sample was observed over the time scale of the experiments.

Results and Discussion

Model Verification

Figure 4 compares the simulated steady-state absorption and fluorescence spectra with those obtained experimentally. The result for the free chains (Figure 4a) shows reasonable agreement, although there are quantitative discrepancies, which are not unexpected given the simplicity of the model. While the experimental absorption band is broader than that of the simulations, the onset of absorption at the red edge

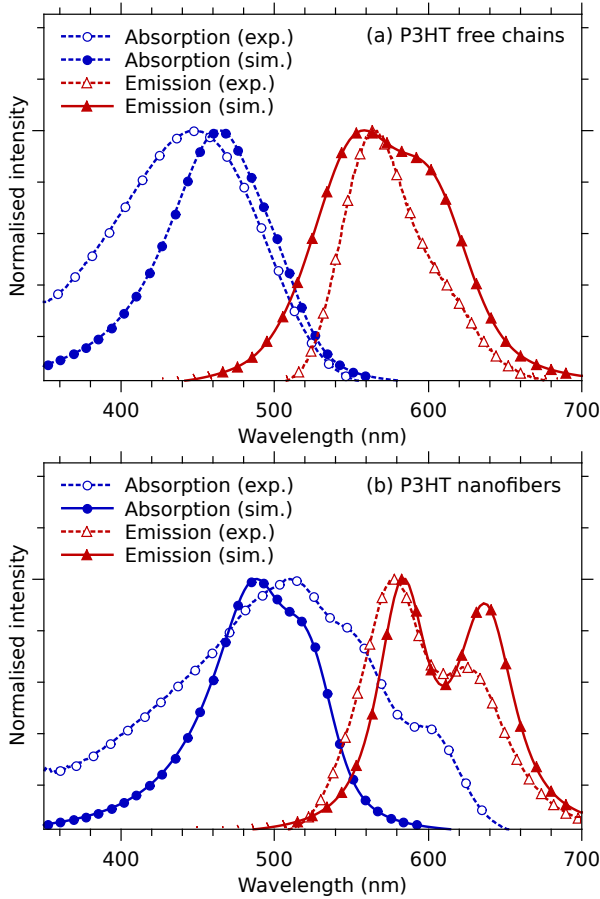


Figure 4: Experimental and simulated steady-state absorption and emission spectra for (a) P3HT free chains and (b) nanofibers.

matches well. It is in this low-energy region that the absorption is dominated by LEGSs, indicating that the energies determined from the Frenkel–Holstein model for these states are reasonable. The fluorescence peak of the free chains is also well simulated, showing that the relaxation energies of the LEGSs are also valid. The small shoulder present in the experimental fluorescence peak is reproduced, but somewhat exaggerated in the simulation data, indicating an overestimation of the intensity of the 0–1 vibronic transition.

The experimental absorption and emission spectra of nanofibers (Figure 4b) exhibit distinct vibronic structure that is also present in the simulated spectra. In particular, the nanofiber emission shows the two characteristic 0–0 and 0–1 transitions associated with H- and J-type aggregate behavior.⁶² These two distinct peaks are reproduced in the simulation data,

despite the intensity of the 0–1 transition again being overestimated. The simulated absorption spectrum is also significantly narrower than the experimental nanofiber spectrum. Some of this discrepancy may be due to only relatively small aggregates being simulated rather than complete nanofibers, so that the full distribution of absorbing chromophores may not be captured. On the other hand, agreement is better for the emission spectrum, since emission is expected to occur from a small number of low-energy chromophores as a result of energy funneling due to exciton transfer, which the simulations are more successfully able to capture.

Importantly, the red-shifting of the absorption and emission peaks in the nanofiber simulations with respect to those in the free chain simulations is captured, indicating that the Frenkel–Holstein model is responding to the structural differences between the two systems and reproducing reasonable energies of the absorptive and emissive chromophores. This result also indicates that the coarse-grained structural model underlying the exciton model accurately captures the structural changes, such as increases in conjugation length, that occur as a result of chain aggregation in P3HT.

The exciton transport simulations are also able to reproduce the dynamics of time-resolved fluorescence upconversion experiments (see Supporting Information), which show a dynamic red-shift in the emission occurring over a period of tens of picoseconds, on a time scale that has been attributed to exciton transport,^{63–65} with different wavelength dependencies for free chains and nanofibers. This result implies the exciton hopping rates calculated in the simulation agree with experimental observations.

Exciton Transport Mechanism

Figure 5 shows the mean squared displacement of excitons over time in the free chain and nanofiber systems. The motion of excitons is not clearly diffusive, with an upper limit to exciton displacement being reached asymptotically due to the finite size of the polymer in which the exciton can travel. The free chains are in dilute

solution, which means that chains are generally well isolated from each other. This puts an upper limit on exciton travel distance, equal to the chain contour length. In reality, chains are not fully extended, nor are excitations exclusively at the chain termini. The nanofiber aggregates are naturally much larger than a single chain, which immediately allows for greater exciton travel. However, the total displacement is still limited to 7–8 nm due to trapping effects coupled with the total exciton lifetime governed by the chromophore radiative rates (eq 12). This result from the simulations is in good agreement with the experimental values for exciton diffusion length in crystalline P3HT.⁶⁶

The difference in the mean squared displacements between the free chains and nanofibers correlates with the distribution of hop counts for each system, shown in Figure 6. On isolated chains the probability that hopping does not occur, where excitation and emission occur from the same chromophore, is approximately 35%. Where hopping does take place, it is likely that only one or two hops will occur, with the probability of an exciton undergoing more than four hops being negligible. This observation is consistent with single-molecule polarization spectroscopy experiments on disordered P3HT,^{67,68} for which the decay of the correlation between excitation and emission polarizations suggests some degree of energy funneling to the lowest energy chromophore, but the lack of perfect anisotropy in the single-molecule emission indicates incomplete funneling to the

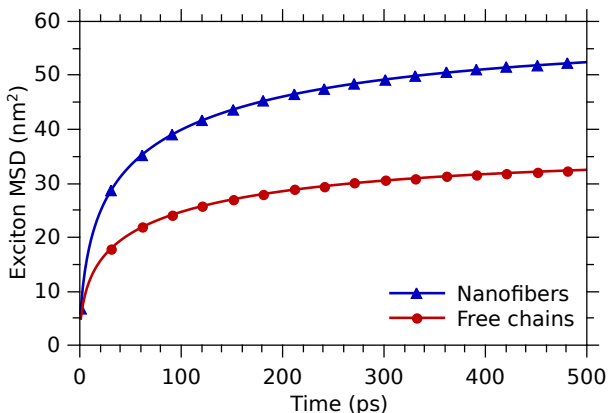


Figure 5: Mean squared displacement (MSD) of excitons in P3HT free chains and nanofibers.

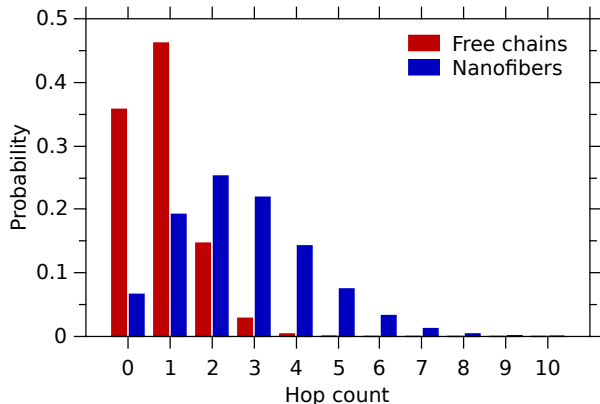


Figure 6: Distributions of total number of hops performed by excitons during the simulations.

lowest energy chromophore. The appearance of broad, homogeneous emission spectra from individual molecules also suggests that emission occurs from a variety of chromophores in the molecule. This can be rationalized from the exciton transport simulations, in which the extended and disordered nature of the free chains can cause a relatively large distance and unfavorable orientation between chromophores, preventing the exciton from reaching the lowest energy site prior to emission. As expected, excitons are more mobile in the nanofibers, with only around 5% of excitons emitting from the initially excited chromophore, as shown in Figure 6. Polymer aggregation clearly leads to a larger selection of chromophores in close proximity and allows for a greater selection of lower energy acceptor sites as possible hop destinations.

Exciton hopping events can be categorized as either intra- or interchain. The proportions of each for the free chains and nanofibers are shown in the inset of Figure 7. The isolation of the free chains is again evident with hops being almost exclusively within the same chain. For the nanofibers there is a predominance of interchain-type hops, indicating that there are either a greater number of interchain acceptor chromophores in the vicinity, or that they are more strongly coupled by a smaller distance or more favorable orientation (eq 9). Analysis of the intrachain-type hops in Figure 7 shows that, for both systems, exciton transfer to the nearest-neighbor chromophore is pre-

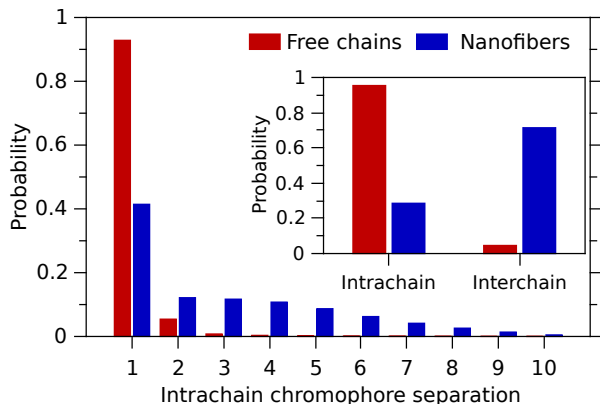


Figure 7: Probability distribution of intrachain hops to neighboring chromophores as a function of intrachain hopping distance in units of chromophore numbers (a value of one equates to a nearest-neighbor hop to an immediately adjacent chromophore, with large values indicating hops to a chromophore at the opposite end of the chain). *Inset*: Probability that an exciton hop is of intrachain or interchain type.

ferred. As the immediately adjacent acceptor chromophore is likely to be both spatially close and possess a favorable orientation with respect to the donor, this result is expected. Similarly, for the free chains, hops to more distant chromophores become increasingly unlikely due to the extended and disordered nature of the chains.

However, with nanofibers the trend for exciton hops between the donor and acceptor separated by two or more chromophores is more complex. The probability of exciton hopping to a site two chromophores away is significantly less than that for a nearest-neighbor type hop, but the probability of hops to sites further along the chain then tapers off slowly. The particular nature of the chain folding is responsible for the above phenomena. A chain that contributes to a nanofiber is likely to fold into segments of length ~ 25 nm. As shown in Figure 8b, these segments are divided into roughly two or three chromophores (chromophores in a free chain are shown in Figure 8a for comparison). The remainder of the chain folds back upon itself. The result is that beyond the directly adjacent chromophore, there is a good chance the remainder of the chain is folded back in close prox-

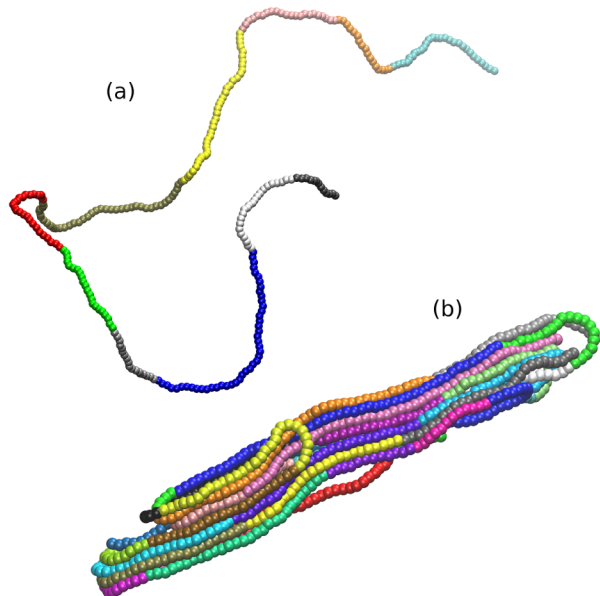


Figure 8: Division of polymer chains into spectroscopic units for (a) a free chain and (b) a nanofiber aggregate. Chromophore colours are arbitrary and alkyl sidechains are not shown for clarity.

imity. Indeed a plot of Euclidean distance between chromophores on a chain against their separation number along the chain (Figure 9a) shows that a chromophore at the opposite end of a chain in a nanofiber aggregate is generally not any more spatially distant than any other on that chain. Furthermore, if hopping events are analyzed (Figure 9b), it can be seen that hops to the nearest-neighbor chromophore in nanofiber aggregates in fact have, on average, the furthest hop distance, and that hops to chromophores elsewhere on the chains are likely due to them being wrapped and aligned closer than the directly adjacent neighbor along the chain. Overall, the results show preference for exciton migration across the chains in nanofiber aggregates rather than along them, most likely in the π -stacking direction due to the close proximity and hence stronger interchain coupling in this direction.^{6,52} Nevertheless, nearest-neighbor hops are the most common intrachain transitions in the nanofiber aggregates due to the favorable correlated orientation of the transition dipoles of adjacent chromophores along the chain.

The extended structure of free chains is ev-

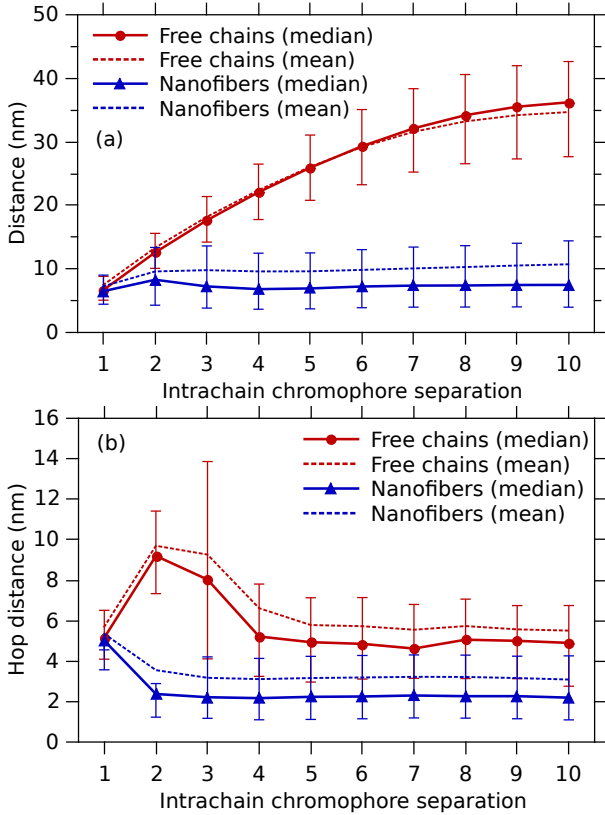


Figure 9: Euclidean distance (a) between intrachain chromophores and (b) of intrachain exciton hops versus the linear chromophore separation along the chain length. Error bars show the first and third quartile.

ident in Figure 9a, with the Euclidean distance increasing with intrachain chromophore separation. As a consequence, hops to sites on the chain separated by more than two chromophores are highly unlikely (Figure 7), with disorder also making favorable transition dipole alignment less probable. Figure 9b suggests that hops between widely separated chromophores only occurs when the chain ends are occasionally brought close together in space.

Figure 10 shows probability maps of excitation, intermediate visit, and emission events for typical free chain and nanofiber systems. Absorption of the simulated 400-nm laser excitation light occurs relatively evenly throughout the polymer chains, although there are a few higher energy sites that are more likely to absorb. These chromophores are well distributed over the extended free chains, but appear to be localized on the outside of the nanofiber structures. Emission sites are again distributed over

the length of the free chains, but appear to be localized to just a few sites in the nanofiber, with a tendency for emission to occur from within the core of the structure. The category of intermediate visits is where a site is an exciton transition pathway but does not directly absorb or emit photons. There are only a small number of these sites on the free chains, where there is a chromophore of just the right energy bridging a high-energy absorption and low-energy emission site. This low probability is also reflected in Figure 6 for hop counts greater than two. On the nanofiber, the intermediate sites appear to be located between the absorbing sites on the exterior and emissive sites on the interior of the structure. Qualitatively, the heat maps in Figure 10 imply there is an energy funneling effect towards the nanofiber core. This energy-funneling behavior was observed in general for the nanofiber aggregates simulated, as illustrated for a number of other aggregates in the Supporting Information.

To confirm this assertion, individual nanofiber aggregates were identified in the nanofiber systems and exciton migration tracked in relation to the center-of-mass of the aggregate. The aggregates were determined by finding clusters of chromophores defined using a density-based clustering algorithm, DBSCAN.⁶⁹ In this method, an aggregate is firstly located by detecting a minimum of six chromophore centers-of-mass within a sphere of 7 nm diameter, and the boundary of the aggregate is then found when the chromophore density falls below this threshold. The Supporting Information shows a plot of the mean squared displacement of an exciton from the center-of-mass of its originating nanofiber cluster over time, showing there is an overall tendency for energy funneling towards the aggregate center. This effect can be explained by the fact that the polymer chains are more ordered in the aggregate core. The more planar structure of the stacked polymer chains in the core results in a longer conjugation length and therefore lower energy chromophores that make favorable acceptor sites. This is backed by an analysis of chromophore conjugation length and chain planarity as a function of distance from the chromophore cluster's center-of-mass

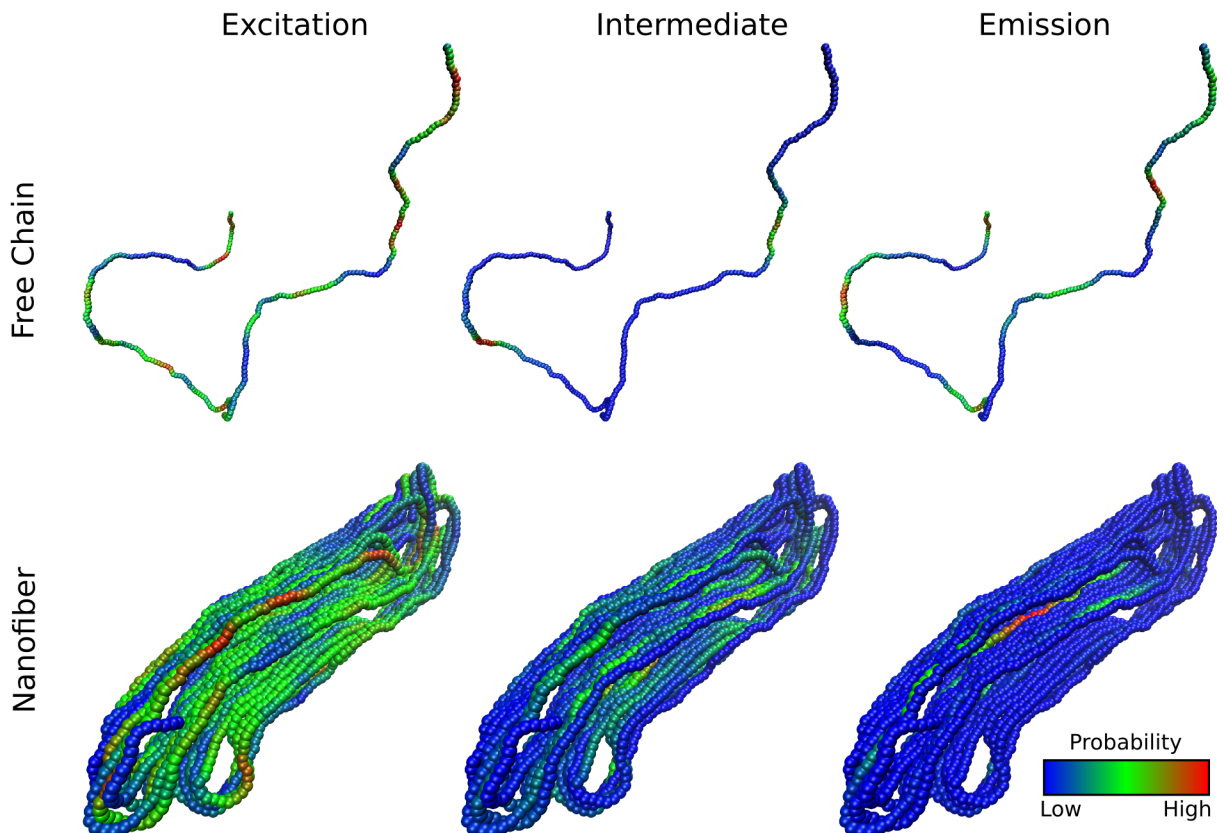


Figure 10: Probability heat maps of excitation, intermediate exciton visit, and emission events on a P3HT free chain and nanofiber aggregate.

(Supporting Information). There is a clear increase in chain planarity closer to the cluster center of mass, with a resulting increase in conjugation length of approximately four thiophene units.

The tendency for excitons to migrate towards the centers of the aggregates has negative implications for charge generation in conjugated polymer solar cells, where exciton migration to and dissociation at the donor–acceptor interface is required. It could be expected that nanofiber-based solar cells would provide greater efficiency than traditional bulk-heterojunction types due to higher charge-carrier mobilities and fiber diameters being comparable to the exciton diffusion length, but these solar cells do not automatically show significant improvements over disordered bulk-heterojunction cells.^{70–72} Furthermore, more recently developed polymers for photovoltaic applications display high efficiency with amorphous microstructures, with any thermal annealing to induce donor–acceptor phase sepa-

ration reducing their performance.^{3,73} Our simulation results suggest that a contributing factor to the poor performance of photovoltaic devices containing relatively large ordered aggregates is the presence of low-energy trap sites at aggregate cores that funnel excitons away from donor–acceptor interfaces and where exciton recombination eventually occurs. This effect may also be responsible for the unexpectedly high fluorescent quantum yields of conjugated polymer nanoparticle suspensions in water, where the water would otherwise be expected to efficiently quench excitons.^{35,74,75} If the exciton is rapidly funneled from the surface towards the low-energy center of the nanoparticle it would then be effectively protected from the aqueous environment.

The individual nanofiber aggregates identified from the coarse-grained P3HT configurations all show some degree of order, but are never perfectly crystalline. Several structural motifs are observed, similar to what has been reported previously in both computational work

and single-molecule spectroscopic experiments on conjugated polymers.^{30,67,68,76,77} Notable extremes are “hairpin”-type structures, with regular, linear folding of chains like that shown in Figure 1c, and “helices” with a more cylindrical stacking of the chains. To investigate whether these structural differences impact the simulation results, the individual aggregates were isolated using the clustering algorithm described above and sorted using a measure of static anisotropy defined by⁷⁶

$$r_s = \frac{1}{n_a} \sum_i \cos^2(\theta_i), \quad (13)$$

where θ_i is the angle between the transition dipole moment vector on monomer i and the sum of transition dipole moment vectors of all monomers in the aggregate and n_a is the number of monomers in the aggregate. The top and bottom $\sim 30\%$ most anisotropic aggregates were then designated as “hairpins” and “helices”, respectively, and exciton transport simulations carried out for each group separately. No significant differences between the simulation results was observed, with the exception of the fluorescence anisotropy data shown in Figure 11b. This difference is expected, as the helical aggregates are more isotropic by definition and should result in greater depolarization of fluorescence as exciton hopping occurs. Interestingly, fitting of the anisotropy decays in Figure 11a and Figure 11b (Supporting Information) shows that the rate of depolarization is similar in both forms of nanofibers as well as in the free chains (~ 7 ps), with only the magnitude of the final depolarization differing. This result is consistent with experimental observations, in which there is little difference between the depolarization rates of free chains and nanofibers, and although the decay time constants are shorter than those of the simulation (~ 2 ps), they are of the same order of magnitude.

The similarity in the rates of depolarization is initially unexpected considering the greater mobility of excitons in the nanofibers than in the free chains (Figure 5). A comparison of the rate of depolarization with that of exciton diffusion is given in the Supporting Information.

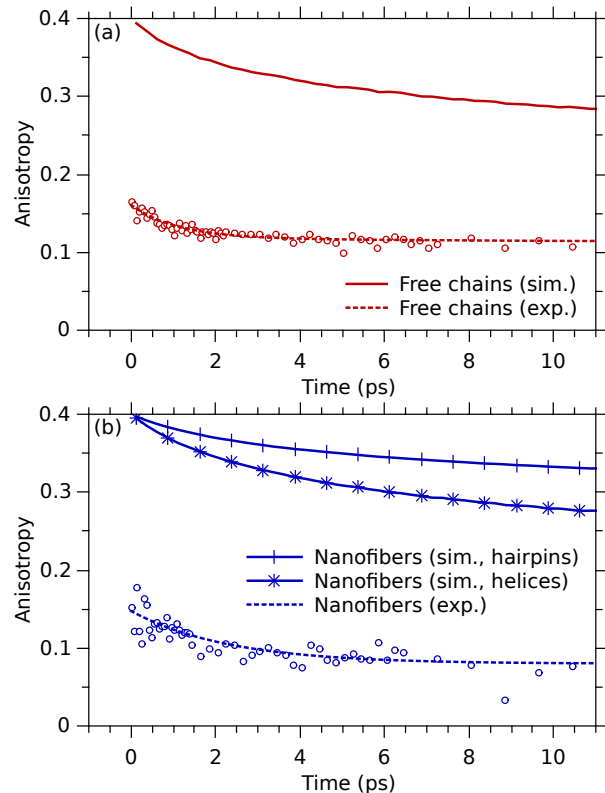


Figure 11: Experimental and simulated fluorescence anisotropy. The measured wavelength is that of the respective fluorescence peak of the sample for both experimental and simulation data (570 nm for free chains and 600 nm for the nanofibers).

The simulations indicate that excitons in nanofibers move on average 40% further than those in free chains for the same amount of fluorescence depolarization. This result can be rationalized by considering that although excitons undergo more hops and travel further in the nanofibers, the ordered alignment of the chains acts to better preserve the direction of the transition dipole moment. The end result is a similar rate of fluorescence depolarization in nanofibers and free chains despite the higher exciton diffusion rate in the nanofibers. Note that in both the simulation and experimental data the rates of depolarization are consistent with those previously attributed to exciton energy-transfer processes.^{63–65}

The experimental fluorescence anisotropy data in Figure 11 show ultrafast depolarization occurring in both the free chains and nanofibers on a time scale of < 100 fs, be-

low the response time of the instrument. This differs from the simulation data, in which the anisotropy has an initial value of 0.4, indicating perfect correlation of the excitation and emission polarizations. Ultrafast fluorescence depolarization is routinely observed in conjugated polymers,^{12,63,78} and has been attributed to geometrical changes in the polymer due to the strong coupling between the electronic and the nuclear degrees of freedom.^{79,80} Correspondingly, relaxation of the initially generated, delocalized states (QEESs) to more localized ones (LEGSs) occurs on the time scale of the nuclear motion, causing rapid change in the direction transition dipole moment as the wavefunction evolves over the disordered chain.^{28,81}

The absence of the ultrafast depolarization effect in the simulation data highlights some deficiencies in the model. While the higher energy eigenstates of eq 1 (QEESs) contribute to the simulated absorption spectrum (Figure 4), it is only the LEGSs that are selected for excitation during the Monte Carlo hopping simulation since, as stated previously, the QEESs rapidly relax to the LEGS with maximum wavefunction overlap. Implementing this behavior would account for some proportion of the ultrafast fluorescence depolarization. An additional contribution to the ultrafast depolarization may be due to delocalization of the initially formed exciton across adjacent chain segments, another effect that is not considered in the simulation model. This could also account for the slightly greater magnitude of depolarization seen in the experimental nanofiber data, in spite of the nanofibers having greater structural order than the free chains. The lack of these ultrafast depolarization effects in the model is not expected to affect the longer time-scale exciton dynamics that is more relevant for energy transfer in organic electronic devices. However, the contribution of geometrical changes to the fluorescence depolarization are harder to quantify as the coarse-grained molecular dynamics that provides the polymer geometry is decoupled from the simulation of the exciton. A static polymer conformation over the lifetime of the exciton is clearly not entirely realistic, but attempting to closely couple the exciton behav-

ior and the molecular dynamics would require extreme computational costs that would limit application of the model to small system sizes.

Conclusions

In summary, we have used accurate coarse-grained molecular dynamics simulations to generate large, 100-chain systems of regioregular P3HT in two contrasting solvent environments made by modifying the implicit solvent model. Free chains characterized by an extended, disordered conformation were produced in a good solvent and were well isolated in a dilute solution. A marginal solvent and polymer concentrations between ~ 0.1 and 2.0 wt% resulted in the formation of nanofiber-like aggregates, which exhibited a semicrystalline microstructure. From these systems, a Frenkel–Holstein exciton model was then applied to calculate wavefunctions and energies of chromophores, with parameters derived from quantum chemical calculations. Finally, Monte Carlo simulations of Förster-type exciton migration were performed using the Fermi Golden Rule with chromophore couplings determined by the line-dipole approximation, in which point-dipole interactions between monomer transition dipoles are summed.

The results of the simulations provide reasonable quantitative agreement with experimental steady-state and time-resolved fluorescence data for P3HT nanofibers and solutions. Simulated exciton diffusion lengths are also in agreement with literature experimental data. Furthermore, morphology-dependent mechanisms of exciton transport were observed on the molecular level. Notably, exciton transfer through the nanofiber aggregates occurred generally by interchain hops towards low-energy sites at the core of the aggregate. These “trap” sites are formed due to the higher level of crystallinity resulting in more planar chains and longer chromophore conjugation lengths. This structure-dependent energy funneling has implications for exciton diffusion to donor–acceptor interfaces in bulk-heterojunction organic solar cells, particularly those employing

polymer nanofibers, and for fluorescence yields of conjugated polymer nanoparticles used in fluorescence imaging. Similar rates of fluorescence depolarization were observed in P3HT free chains and nanofibers in both experimental and simulation data, in spite of exciton mobility being much greater in the nanofibers. This phenomena can be rationalized by the fact that the increased order of the chromophore orientations acts as a counterbalance to help preserve the fluorescence polarization.

Our methods demonstrate a bridging of the gap between highly accurate atomistic quantum calculations and generalized lattice models of conjugated polymers. A combination of meso-scale models provides realistic polymer conformations and gives molecular-level detail of exciton transport in conjugated polymers on experimentally relevant length and time scales.

Acknowledgement The authors acknowledge Dr. William Barford for providing an early version of his exciton transport simulation code. This research was undertaken with the assistance of resources provided at the NCI National Facility systems at the Australian National University through the National Computational Merit Allocation Scheme supported by the Australian Government. Computational resources provided by eResearch SA are also gratefully acknowledged.

Supporting Information Available: Time-resolved fluorescence data, quantitative analysis of exciton migration to core of nanofibers, additional event heat map figures, fluorescence anisotropy fitting parameters, and oligomer $S_0 \rightarrow S_1$ transition energies. This material is available free of charge via the Internet at <http://pubs.acs.org/>.

References

- (1) Brabec, C. J.; Gowrisanker, S.; Halls, J. J. M.; Laird, D.; Jia, S.; Williams, S. P. Polymer–Fullerene Bulk-Heterojunction Solar Cells. *Adv. Mater.* **2010**, *22*, 3839–3856.
- (2) Perepichka, I.; Perepichka, D.; Meng, H.; Wudl, F. Light-Emitting Polythiophenes. *Adv. Mater.* **2005**, *17*, 2281–2305.
- (3) Zhao, B.; He, Z.; Cheng, X.; Qin, D.; Yun, M.; Wang, M.; Huang, X.; Wu, J.; Wu, H.; Cao, Y. Flexible Polymer Solar Cells with Power Conversion Efficiency of 8.7%. *J. Mater. Chem. C* **2014**, *2*, 5077–5082.
- (4) Chen, C.-C.; Dou, L.; Zhu, R.; Chung, C.-H.; Song, T.-B.; Zheng, Y. B.; Hawks, S.; Li, G.; Weiss, P. S.; Yang, Y. Visibly Transparent Polymer Solar Cells Produced by Solution Processing. *ACS Nano* **2012**, *6*, 7185–7190.
- (5) Mulligan, C. J.; Bilén, C.; Zhou, X.; Belcher, W. J.; Dastoor, P. C. Levelised Cost of Electricity for Organic Photovoltaics. *Sol. Energ. Mat. Sol. Cells* **2015**, *133*, 26–31.
- (6) Schwartz, B. J. Conjugated Polymers as Molecular Materials: How Chain Conformation and Film Morphology Influence Energy Transfer and Interchain Interactions. *Annu. Rev. Phys. Chem.* **2003**, *54*, 141–172.
- (7) Vanlaeke, P.; Swinnen, A.; Haeldermans, I.; Vanhoyland, G.; Aernouts, T.; Cheyns, D.; Deibel, C.; DaHaen, J.; Heremans, P.; Poortmans, J. et al. P3HT/PCBM Bulk Heterojunction Solar Cells: Relation Between Morphology and Electro-Optical Characteristics. *Sol. Energ. Mat. Sol. Cells* **2006**, *90*, 2150–2158.
- (8) McNeill, C. R.; Westenhoff, S.; Groves, C.; Friend, R. H.; Greenham, N. C. Influence of Nanoscale Phase Separation on the Charge Generation Dynamics and Photovoltaic Performance of Conjugated Polymer Blends: Balancing Charge Generation and Separation. *J. Phys. Chem. C* **2007**, *111*, 19153–19160.
- (9) Pivrikas, A.; Neugebauer, H.; Sariciftci, N. S. Influence of Processing Additives to Nano-Morphology and Efficiency

- of Bulk-Heterojunction Solar Cells: A Comparative Review. *Sol. Energ.* **2011**, *85*, 1226–1237.
- (10) Beljonne, D.; Cornil, J.; Muccioli, L.; Zannoni, C.; Brédas, J.-L.; Castet, F. Electronic Processes at Organic–Organic Interfaces: Insight from Modeling and Implications for Opto-electronic Devices? *Chem. Mater.* **2011**, *23*, 591–609.
- (11) Darling, S. B. Isolating the Effect of Torsional Defects on Mobility and Band Gap in Conjugated Polymers. *J. Phys. Chem. B* **2008**, *112*, 8891–8895.
- (12) Dykstra, T. E.; Hennebicq, E.; Beljonne, D.; Gierschner, J.; Claudio, G.; Bittner, E. R.; Knoester, J.; Scholes, G. D. Conformational Disorder and Ultrafast Exciton Relaxation in PPV–Family Conjugated Polymers. *J. Phys. Chem. B* **2009**, *113*, 656–667.
- (13) Singh, J.; Bittner, E. R.; Beljonne, D.; Scholes, G. D. Fluorescence Depolarization in Poly[2-methoxy-5-((2-ethylhexyl)oxy)-1,4-phenylenevinylene]: Sites Versus Eigenstates Hopping. *J. Chem. Phys.* **2009**, *131*, 194905.
- (14) Cheung, D. L.; McMahon, D. P.; Troisi, A. A Realistic Description of the Charge Carrier Wave Function in Microcrystalline Polymer Semiconductors. *J. Am. Chem. Soc.* **2009**, *131*, 11179–11186.
- (15) Munoz-Losa, A.; Curutchet, C.; Galvan, I. F.; Mennucci, B. Quantum Mechanical Methods Applied to Excitation Energy Transfer: A Comparative Analysis on Excitation Energies and Electronic Couplings. *J. Chem. Phys.* **2008**, *129*, 034104.
- (16) Rühle, V.; Lukyanov, A.; May, F.; Schrader, M.; Vehoff, T.; Kirkpatrick, J.; Baumeier, B.; Andrienko, D. Microscopic Simulations of Charge Transport in Disordered Organic Semiconductors. *J. Chem. Theory Comput.* **2011**, *7*, 3335–3345.
- (17) Denis, J.-C.; Schumacher, S.; Galbraith, I. Quantitative Description of Interactions Between Linear Organic Chromophores. *J. Chem. Phys.* **2012**, *137*, 224102.
- (18) Groves, C. Developing Understanding of Organic Photovoltaic Devices: Kinetic Monte Carlo Models of Geminate and Non-Geminate Recombination, Charge Transport and Charge Extraction. *Energy Environ. Sci.* **2013**, *6*, 3202–3217.
- (19) Kordt, P.; Stenzel, O.; Baumeier, B.; Schmidt, V.; Andrienko, D. Parametrization of Extended Gaussian Disorder Models from Microscopic Charge Transport Simulations. *J. Chem. Theory Comput.* **2014**, *10*, 2508–2513.
- (20) Noriega, R.; Salleo, A.; Spakowitz, A. J. Chain Conformations Dictate Multiscale Charge Transport Phenomena in Disordered Semiconducting Polymers. *Proc. Natl. Acad. Sci. USA* **2013**, *110*, 16315–16320.
- (21) Bittner, E. R.; Silva, C. Noise-Induced Quantum Coherence Drives Photo-Carrier Generation Dynamics at Polymeric Semiconductor Heterojunctions. *Nat. Commun.* **2014**, *5*, 3119.
- (22) Maturová, K.; van Bavel, S. S.; Wienk, M. M.; Janssen, R. J.; Kemmerink, M. Description of the Morphology Dependent Charge Transport and Performance of Polymer:Fullerene Bulk Heterojunction Solar Cells. *Adv. Funct. Mater.* **2011**, *21*, 261–269.
- (23) Nam, Y. M.; Huh, J.; Ho Jo, W. Optimization of Thickness and Morphology of Active Layer for High Performance of Bulk-Heterojunction Organic Solar Cells. *Sol. Energy Mater. Sol. Cells* **2010**, *94*, 1118–1124.
- (24) Grage, M. M. L.; Wood, P. W.; Ruseckas, A.; Pullerits, T.; Mitchell, W.; Burn, P. L.; Samuel, I. D. W.; Sundstrom, V. Conformational Disorder and

- Energy Migration in MEH-PPV with Partially Broken Conjugation. *J. Chem. Phys.* **2003**, *118*, 7644–7650.
- (25) Westenhoff, S.; Daniel, C.; Friend, R. H.; Silva, C.; Sundstrom, V.; Yartsev, A. Exciton Migration in a Polythiophene: Probing the Spatial and Energy Domain by Line-Dipole Forster-Type Energy Transfer. *J. Chem. Phys.* **2005**, *122*, 094903.
- (26) Westenhoff, S.; Beenken, W. J. D.; Yartsev, A.; Greenham, N. C. Conformational Disorder of Conjugated Polymers. *J. Chem. Phys.* **2006**, *125*, 154903.
- (27) Tozer, O. R.; Barford, W. Exciton Dynamics in Disordered Poly(p-phenylenevinylene). 1. Ultrafast Interconversion and Dynamical Localization. *J. Phys. Chem. A* **2012**, *116*, 10310–10318.
- (28) Barford, W.; Tozer, O. R. Theory of Exciton Transfer and Diffusion in Conjugated Polymers. *J. Chem. Phys.* **2014**, *141*, 164103.
- (29) Carbone, P.; Troisi, A. Charge Diffusion in Semiconducting Polymers: Analytical Relation between Polymer Rigidity and Time Scales for Intrachain and Interchain Hopping. *J. Phys. Chem. Lett.* **2014**, *5*, 2637–2641.
- (30) Schwarz, K. N.; Kee, T. W.; Huang, D. M. Coarse-Grained Simulations of the Solution-Phase Self-Assembly of Poly(3-hexylthiophene) Nanostructures. *Nanoscale* **2013**, *5*, 2017–2027.
- (31) Onoda, M.; Tada, K.; Zakhidov, A.; Yoshino, K. Photoinduced Charge Separation in Photovoltaic Cell with Heterojunction of P- and N-Type Conjugated Polymers. *Thin Solid Films* **1998**, *331*, 76–81.
- (32) Ihn, K. J.; Moulton, J.; Smith, P. Whiskers of Poly(3-alkylthiophene)s. *J. Polym. Sci. B Polym. Phys.* **1993**, *31*, 735–742.
- (33) Schenning, A. P. H. J.; Meijer, E. W. Supramolecular Electronics; Nanowires from Self-Assembled Pi-Conjugated Systems. *Chem. Commun.* **2005**, 3245–3258.
- (34) Park, D.; Kim, B.; Jang, M.; Bae, K.; Lee, S.; Joo, J. Synthesis and Characterization of Polythiophene and Poly(3-methylthiophene) Nanotubes and Nanowires. *Synth. Met.* **2005**, *153*, 341–344.
- (35) Pecher, J.; Mecking, S. Nanoparticles of Conjugated Polymers. *Chem. Rev.* **2010**, *110*, 6260–6279.
- (36) Barford, W.; Bittner, E. R.; Ward, A. Exciton Dynamics in Disordered Poly(p-phenylenevinylene). 2. Exciton Diffusion. *J. Phys. Chem. A* **2012**, *116*, 10319–10327.
- (37) Marcus, M.; Tozer, O. R.; Barford, W. Theory of Optical Transitions in Conjugated Polymers. II. Real Systems. *J. Chem. Phys.* **2014**, *141*, 164102.
- (38) Samitsu, S.; Shimomura, T.; Heike, S.; Hashizume, T.; Ito, K. Effective Production of Poly(3-alkylthiophene) Nanofibers by means of Whisker Method using Anisole Solvent: Structural, Optical, and Electrical Properties. *Macromolecules* **2008**, *41*, 8000–8010.
- (39) Chernyak, V.; Poliakov, E. Y.; Tretiak, S.; Mukamel, S. Two-Exciton States and Spectroscopy of Phenylacetylene Dendrimers. *J. Chem. Phys.* **1999**, *111*, 4158–4168.
- (40) Avgin, I.; Huber, D. Excitons in Disordered Polymers. *J. Lumin.* **2007**, *122–123*, 389–392.
- (41) Holstein, T. Studies of Polaron Motion: Part II. The “Small” Polaron. *Ann. Phys.* **1959**, *8*, 343–389.
- (42) Holstein, T. Studies of Polaron Motion: Part I. The Molecular-Crystal Model. *Ann. Phys.* **1959**, *8*, 325–342.

- (43) Spano, F. C. Modeling Disorder in Polymer Aggregates: The Optical Spectroscopy of Regioregular Poly(3-hexylthiophene) Thin Films. *J. Chem. Phys.* **2005**, *122*, 234701.
- (44) Spano, F. C. Absorption in Regio-Regular Poly(3-hexylthiophene) Thin Films: Fermi Resonances, Interband Coupling and Disorder. *J. Chem. Phys.* **2006**, *325*, 22–35.
- (45) Barford, W.; Trembath, D. Exciton Localization in Polymers with Static Disorder. *Phys. Rev. B* **2009**, *80*, 165418.
- (46) Malyshev, A. V.; Malyshev, V. A. Statistics of Low Energy Levels of a One-Dimensional Weakly Localized Frenkel Exciton: A Numerical Study. *Phys. Rev. B* **2001**, *63*, 195111.
- (47) Barford, W.; Boczarow, I.; Wharram, T. Ultrafast Dynamical Localization of Photoexcited States in Conformationally Disordered Poly(p-phenylenevinylene). *J. Phys. Chem. A* **2011**, *115*, 9111–9119.
- (48) Makhov, D. V.; Barford, W. Local Exciton Ground States in Disordered Polymers. *Phys. Rev. B* **2010**, *81*, 165201.
- (49) North, A. M.; Ross, D. A. Singlet Energy Migration Down Conjugated Polymer Chains. *J. Polym. Sci. Polym. Symp.* **1976**, *55*, 259–267.
- (50) King, S.; Vaughan, H.; Monkman, A. Orientation of Triplet and Singlet Transition Dipole Moments in Polyfluorene, Studied by Polarised Spectroscopies. *Chem. Phys. Lett.* **2007**, *440*, 268–272.
- (51) Barford, W. Exciton Transfer Integrals Between Polymer Chains. *J. Chem. Phys.* **2007**, *126*, 134905.
- (52) Köse, M. E. Evaluation of Excitonic Coupling and Charge Transport Integrals in P3HT Nanocrystal. *J. Phys. Chem. C* **2011**, *115*, 13076–13082.
- (53) Gierschner, J.; Mack, H.-G.; Lüer, L.; Oelkrug, D. Fluorescence and Absorption Spectra of Oligophenylenevinylenes: Vibronic Coupling, Band Shapes, and Solvatochromism. *J. Chem. Phys.* **2002**, *116*, 8596–8609.
- (54) Scholes, G. D. Long-Range Resonance Energy Transfer In Molecular Systems. *Annu. Rev. Phys. Chem.* **2003**, *54*, 57–87.
- (55) Morfa, A. J.; Barnes, T. M.; Ferguson, A. J.; Levi, D. H.; Rumbles, G.; Rowlen, K. L.; van de Lagemaat, J. Optical Characterization of Pristine Poly(3-hexylthiophene) Films. *J. Polym. Sci. B Polym. Phys.* **2011**, *49*, 186–194.
- (56) Huang, Y.-C.; Lu, T.-C.; Huang, C.-I. Exploring the Correlation Between Molecular Conformation and UV-Visible Absorption Spectra of Two-Dimensional Thiophene-Based Conjugated Polymers. *Polymer* **2013**, *54*, 6489–6499.
- (57) Oliveira, E. F.; Lavarda, F. C. Effect of the Length of Alkyl Side Chains in the Electronic Structure of Conjugated Polymers. *Mater. Res.* **2015**, <http://dx.doi.org/10.1590/1516-1439.278814>.
- (58) Zhao, M.-T.; Singh, B. P.; Prasad, P. N. A Systematic Study of Polarizability and Microscopic Third-Order Optical Nonlinearity in Thiophene Oligomers. *J. Chem. Phys.* **1988**, *89*, 5535–5541.
- (59) Bidan, G.; De Nicola, A.; Enée, V.; Guillerez, S. Synthesis and UV-Visible Properties of Soluble Regioregular Oligo(3-octylthiophenes), Monomer to Hexamer. *Chem. Mater.* **1998**, *10*, 1052–1058.
- (60) Brown, P. J.; Thomas, D. S.; Köhler, A.; Wilson, J. S.; Kim, J.-S.; Ramsdale, C. M.; Siringhaus, H.; Friend, R. H. Effect of Interchain Interactions on the Absorption and Emission of Poly(3-hexylthiophene). *Phys. Rev. B* **2003**, *67*, 64203.

- (61) Tsoi, W. C.; James, D. T.; Kim, J. S.; Nicholson, P. G.; Murphy, C. E.; Bradley, D. D. C.; Nelson, J.; Kim, J.-S. The Nature of In-Plane Skeleton Raman Modes of P3HT and Their Correlation to the Degree of Molecular Order in P3HT:PCBM Blend Thin Films. *J. Am. Chem. Soc.* **2011**, *133*, 9834–9843.
- (62) Spano, F. C.; Silva, C. H- and J-Aggregate Behavior in Polymeric Semiconductors. *Annu. Rev. Phys. Chem.* **2014**, *65*, 477–500.
- (63) Wells, N. P.; Boudouris, B. W.; Hillmyer, M. A.; Blank, D. A. Intramolecular Exciton Relaxation and Migration Dynamics in Poly(3-hexylthiophene). *J. Phys. Chem. C* **2007**, *111*, 15404–15414.
- (64) Xie, Y.; Li, Y.; Xiao, L.; Qiao, Q.; Dhakal, R.; Zhang, Z.; Gong, Q.; Galipeau, D.; Yan, X. Femtosecond Time-Resolved Fluorescence Study of P3HT/PCBM Blend Films. *J. Phys. Chem. C* **2010**, *114*, 14590–14600.
- (65) Banerji, N.; Cowan, S.; Vauthey, E.; Heeger, A. J. Ultrafast Relaxation of the Poly(3-hexylthiophene) Emission Spectrum. *J. Phys. Chem. C* **2011**, *115*, 9726–9739.
- (66) Sim, M.; Shin, J.; Shim, C.; Kim, M.; Jo, S. B.; Kim, J.-H.; Cho, K. Dependence of Exciton Diffusion Length on Crystalline Order in Conjugated Polymers. *J. Phys. Chem. C* **2014**, *118*, 760–766.
- (67) Adachi, T.; Lakhwani, G.; Traub, M. C.; Ono, R. J.; Bielawski, C. W.; Barbara, P. F.; Vanden Bout, D. A. Conformational Effect on Energy Transfer in Single Polythiophene Chains. *J. Phys. Chem. B* **2012**, *116*, 9866–9872.
- (68) Chen, P.-Y.; Rassamesard, A.; Chen, H.-L.; Chen, S.-A. Conformation and Fluorescence Property of Poly(3-hexylthiophene) Isolated Chains Studied by Single Molecule Spectroscopy: Effects of Solvent Quality and Regioregularity. *Macromolecules* **2013**, *46*, 5657–5663.
- (69) Ester, M.; Kriegel, H.-P.; S, J.; Xu, X. A Density-Based Algorithm for Discovering Clusters in Large Spatial Databases with Noise. *Proc. of 2nd In. Conf. on Knowledge Discovery and Data Mining* **1996**, *96*, 226–231.
- (70) Sun, S.; Salim, T.; Wong, L. H.; Foo, Y. L.; Boey, F.; Lam, Y. M. A New Insight into Controlling Poly(3-hexylthiophene) Nanofiber Growth Through a Mixed-Solvent Approach for Organic Photovoltaics Applications. *J. Mater. Chem.* **2011**, *21*, 377–386.
- (71) Kurniawan, M.; Salim, T.; Tai, K. F.; Sun, S.; Sie, E. J.; Wu, X.; Yeow, E. K. L.; Huan, C. H. A.; Lam, Y. M.; Sum, T. C. Carrier Dynamics in Polymer Nanofiber: Fullerene Solar Cells. *J. Phys. Chem. C* **2012**, *116*, 18015–18022.
- (72) Solanki, A.; Wu, B.; Salim, T.; Yeow, E. K. L.; Lam, Y. M.; Sum, T. C. Performance Improvements in Polymer Nanofiber/Fullerene Solar Cells with External Electric Field Treatment. *J. Phys. Chem. C* **2014**, *118*, 11285–11291.
- (73) He, Z.; Zhong, C.; Su, S.; Xu, M.; Wu, H.; Cao, Y. Enhanced Power-Conversion Efficiency in Polymer Solar Cells Using an Inverted Device Structure. *Nat. Photon.* **2012**, *6*, 591–595.
- (74) Wu, C.; Bull, B.; Szymanski, C.; Christensen, K.; McNeill, J. Multicolor Conjugated Polymer Dots for Biological Fluorescence Imaging. *ACS Nano* **2008**, *2*, 2415–2423.
- (75) Clifton, S. N.; Beattie, D. A.; Mierczynska-Vasilev, A.; Acres, R. G.; Morgan, A. C.; Kee, T. W. Chemical Defects in the Highly Fluorescent Conjugated Polymer Dots. *Langmuir* **2010**, *26*, 17785–17789.

- (76) Hu, D.; Yu, J.; Wong, K.; Bagchi, B.; Rossky, P. J.; Barbara, P. F. Collapse of Stiff Conjugated Polymers with Chemical Defects into Ordered, Cylindrical Conformations. *Nature* **2000**, *405*, 1030–1033.
- (77) Bagchi, B. Photochemical Funnel in Stiff Conjugated Polymers: Interplay Between Defect Mediated Polymer Conformations, Side Chain Interactions and Resonance Energy Transfer. *Annu. Rep. Prog. Chem., Sect. C: Phys. Chem.* **2013**, *109*, 36–64.
- (78) Ruseckas, A.; Wood, P.; Samuel, I. D. W.; Webster, G. R.; Mitchell, W. J.; Burn, P. L.; Sundström, V. Ultrafast Depolarization of the Fluorescence in a Conjugated Polymer. *Phys. Rev. B* **2005**, *72*, 115214.
- (79) Yang, X.; Dykstra, T.; Scholes, G. Photon–Echo Studies of Collective Absorption and Dynamic Localization of Excitation in Conjugated Polymers and Oligomers. *Phys. Rev. B* **2005**, *71*, 045203.
- (80) Tapping, P. C.; Kee, T. W. Optical Pumping of Poly(3-hexylthiophene) Singlet Excitons Induces Charge Carrier Generation. *J. Phys. Chem. Lett.* **2014**, *5*, 1040–1047.
- (81) Beenken, W. J. D.; Pullerits, T. Spectroscopic Units in Conjugated Polymers: A Quantum Chemically Founded Concept? *J. Phys. Chem. B* **2004**, *108*, 6164–6169.